physica status solidi pss www.pss-b.com

Check for updates

Si/Ge (111) Semicoherent Interfaces: Responses to an In-Plane Shear and Interactions with Lattice Dislocations

*Shuozhi Xu, Yang Li, and Youping Chen**

Concurrent atomistic–continuum simulations are employed to study Si/Ge (111) semicoherent interfaces in terms of their responses to an in-plane shear and interactions with lattice dislocations. Three types of Si/Ge interfaces, differing in interfacial structures and energy, are considered. Type I interface coincides with the shuffle-set slip plane and contains a hexagonal network of edge dislocations. Type II and Type III interfaces both coincide with the glide-set slip plane, yet they contain, respectively, a triangular and a hexagonal network of Shockley partial dislocations. The simulations show that among the three types of interfaces, 1) Type I interface is the least stable subject to an in-plane shear and 2) Type III interface impedes the gliding of lattice dislocations the most significantly.

1. Introduction

Multilayered crystalline materials containing semicoherent interfaces usually possess ultra-high strength and hardness.[1] Their superior mechanical properties are mainly attributed to the misfit dislocation networks formed at the interfaces to accommodate the lattice mismatch-induced strain between the two materials, as the layer thickness exceeds a critical value.[2] The heterostructures containing misfit dislocation networks can be obtained by a variety of techniques, including chemical vapor deposition, molecular beam epitaxy, and surfactant-mediated epitaxial growth.[3] The misfit dislocation networks play an important role in the mechanical responses of the multilayered materials.[4] When a ferrite/cementite interface is subject to an in-plane shear, recent atomistic simulations showed that the specific inelastic deformation mode, e.g., dislocation nucleation or intergranular fracture, depends on the structures[5] and spacings[6] of the misfit dislocation network. Besides the in-plane shear, another common phenomenon that occurs in strained multilayered materials is the interactions between lattice dislocations and interfaces. In most, if not all, cases, the interfaces act as barriers to the gliding of lattice dislocations, resulting in an increase in the yield strength. Based on the Peierls model and atomistic simulations, Anderson et al.[7] found that the misfit dislocations at an Al/Ni interface contribute to ≈50% of the total impedance of the lattice dislocations by the interface. A Peierls–Nabarro model-based simulation by Shehadeh et al.[8] revealed that in a Cu/Ni bicrystal, the competition between the dislocation spreading within the interface and the dislocation transmission across the interface depends on the characteristics of the excess energy landscape associated with the interface. Using atomistic simulations, Cheng et al.[9] showed that when a Cu/Ni bilayer is subject to nanoscratching with an intermediate normal load, the misfit dislocation network becomes a significant barrier to the scratching-induced lattice dislocations, hence decreasing the frictional coefficient. More recently, Zhu et al.[10] conducted atomistic simulations in a Ni/Ni_3Al system. They found that the interfacial Lomer–Cottrell locks and dislocation junctions prevent lattice dislocations that originate in Ni from gliding into Ni_3Al directly.

Compared with those in metals, semicoherent interfaces in semiconductors are much less studied. An example is the Si/Ge multilayer, a common semiconductor.[11] It is known that Ge can grow epitaxially on Si {100}, {110}, {111}, and {112} surfaces.[12] The Frank–Bilby theory[13,14] provides a way to determine the continuous distribution of interface Burgers content. However, atoms within the actual interface tend to form discrete dislocations to minimize the interfacial energy.[15] The characters of the interface discrete dislocations, such as the line sense, Burgers vector, and spacing, cannot be determined by the Frank–Bilby theory.[16] Therefore, experiments using electron microscopy and/or atomistic simulations are usually employed.[17] Among the four main crystallographic orientations of the Si/Ge interfaces, the {111} interface is unique in that three types of misfit dislocation networks have been identified in experiments.[18] We elect to investigate the Si/Ge {111} interfaces, because it would be interesting to explore the responses of different misfit dislocation networks to the same in-plane shear and their interactions with the same lattice dislocations, whereas the crystallographic orientations of the interfaces are the same.

Furthermore, the three types of Si/Ge {111} interfaces are termed Types I, II, and III, respectively. Type I interface involves a network of perfect edge dislocations,[19] in agreement with the prediction by the O-lattice theory.[20] Type II and Type III interfaces, respectively, contain a triangular network[21] and a hexagonal network[22] of 90° Shockley partial dislocations. All three

Dr. S. Xu
California NanoSystems Institute
University of California, Santa Barbara
Santa Barbara, CA 93106-6105, USA

Dr. Y. Li, Prof. Y. Chen
Department of Mechanical and Aerospace Engineering
University of Florida
Gainesville, FL 32611, USA
E-mail: ypchen2@ufl.edu

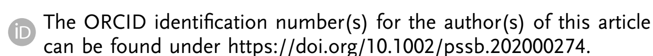
The ORCID identification number(s) for the author(s) of this article can be found under https://doi.org/10.1002/pssb.202000274.

DOI: 10.1002/pssb.202000274

 © 2020 Wiley-VCH GmbH

types of dislocation networks have been reproduced by atomistic simulations in Si/Ge bilayers.[23,24] However, behaviors of these interfaces in strained Si/Ge systems have not been studied, to the best of our knowledge. As a result, the mechanical properties of Si/Ge multilayers are not well understood. A prior atomistic simulation investigated the transmission of lattice dislocations across a Si/Ge (100) coherent interface,[25] but not a (111) semi-coherent interface.

In this article, we explore the three types of misfit dislocation networks at the Si/Ge (111) interface in terms of the responses to an in-plane shear and interactions with lattice dislocations. From the perspective of simulations, the interfacial structures may be well reproduced using relatively small simulation cells, yet phenomena that involve lattice dislocations must be based on sufficiently large cells due to the long-range stress fields of these dislocations. On the other hand, modeling the inelastic deformation of interfaces and lattice dislocation/interface interactions necessitates an accurate description of the short-range dislocation core structures that are critical in these situations. Therefore, we resort to the concurrent atomistic–continuum (CAC) method,[26–28] which has been demonstrated as an effective tool in simulating multiple dislocation-mediated plasticity problems in various material systems, including metals (e.g., Ag,[29] Al,[30] Au,[31] Cu,[32] Ni,[33] and W[34]), ceramics (e.g., $SrTiO_3$[35]), and semiconductors (e.g., Si,[36] PbTe, and PbSe[37]). Relevant to the current work, CAC has been used to investigate misfit dislocations in PbTe/PbSe heteroepitaxial systems,[37] dislocation nucleation from grain boundaries (GBs) in a ceramic,[35] and dislocation/GB interactions in metals.[38,39] The success of these CAC simulations suggests the applicability of this approach to interfacial shearing and dislocation/interface interactions in semiconductors.

2. Methodology

Figure 1 presents the schematic of the CAC model of an unrelaxed Si/Ge bicrystal. Crystallographic orientations along the x-, y-, and z-directions, respectively, are $[10\bar{1}]$, $[1\bar{1}0]$, and $[0\bar{1}\,\bar{1}]$. Note that the three axes are not perpendicular to each other. The edge lengths of the simulation cell along the three axes are 153.5, 153.5, and 339.6 nm, respectively. Traction-free boundary conditions are applied along all three directions. Along the z-axis, the cell is equally partitioned into two crystals: Si and Ge, between them lies a (111) interface that is within the xy plane. Interatomic interactions in Si,[40] Ge,[41] and those between Si and Ge[42] are described using three Stillinger–Weber (SW) potentials. The lattice parameters $a_0 = 0.543$ and 0.566 nm, respectively, in Si and Ge. We remark that the same SW potential for Si has been used in a prior CAC simulation[36] in which the hexagonal shape of shuffle dislocation loops was correctly reproduced.

The 3D finite elements with each of which containing 1024 atoms are used in the CAC model, except in the regions within 2.2 nm from the interfaces, for which atomistic domains are meshed to render the interfacial structures in atomic resolution. Note that 1) discontinuities exist between adjacent finite elements to allow for dislocations, and 2) the thickness of the atomistic domain was shown to be sufficient for the CAC model to yield the same interfacial structure as a fully resolved atomistic

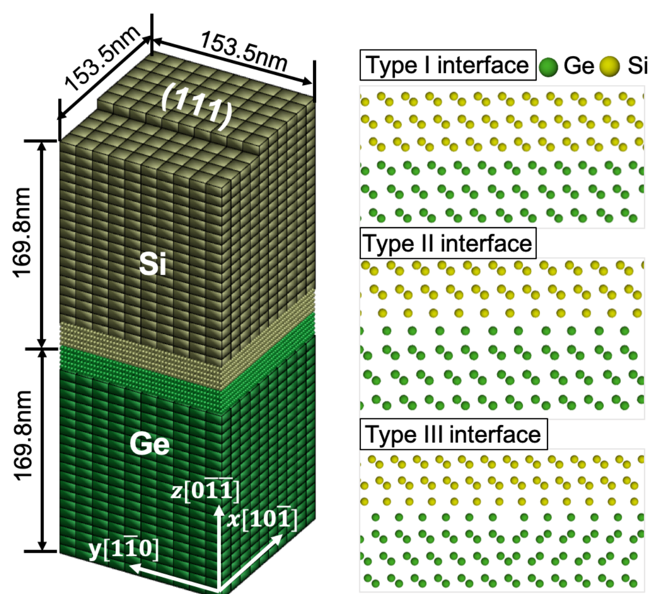

Figure 1. Left: The schematic of the CAC model of an unrelaxed Si/Ge bicrystal containing a (111) interface. Right: Exploded views of the interface region in the three initial models of the three types of interfaces. Atomistic domains are meshed in regions within 2.2 nm along the z-direction from the interface. Used elsewhere are 3D rhombohedral finite elements each of which contains 1024 atoms. Note that the (111) interface is within the xy plane. The three axes (x, y, and z) are not perpendicular to each other.

model.[35] As a result, the simulation cell contains 0.37 million finite elements and 7.4 million atoms. As each finite element has eight nodes and each node is associated with two atoms, the total number of degrees of freedom (DOFs) is 39.96 million. Compared with an equivalent fully resolved atomistic model, which would contain 1.13 billion DOFs, our CAC model reduces the number of DOFs by 96.47%. Three types of Si/Ge interfaces are considered: Type I interface coincides with the shuffle-set slip plane, whereas Type II and Type III interfaces coincide with the glide-set slip plane. Type III interface is built on Type II interface by rotating and translating some atoms in the latter following the previous study.[24] Configurations containing both finite elements and atoms are visualized using Tecplot. At the interfaces, the misfit dislocation networks are identified using a dislocation extraction algorithm (DXA)[43] and visualized in OVITO.[44]

All dynamic CAC simulations in this work are low-temperature simulations, in which thermal fluctuations with wavelength smaller than the size of the finite elements are ignored, and a time step size of 0.01 ps is adopted. The interactions between nodes in the finite elements and atoms in the atomistic domains are realized by a unified atomistic–continuum integral formulation. At each time step, the force on each node is calculated based on the interatomic potential, which serves as the only constitutive law. In parallel, the force on each atom in the atomistic domain is obtained also based on the interatomic potential, as in molecular dynamics (MD). These forces are then used to update the accelerations, velocities, and eventually positions of nodes and atoms.[45,46] As a

© 2020 Wiley-VCH GmbH

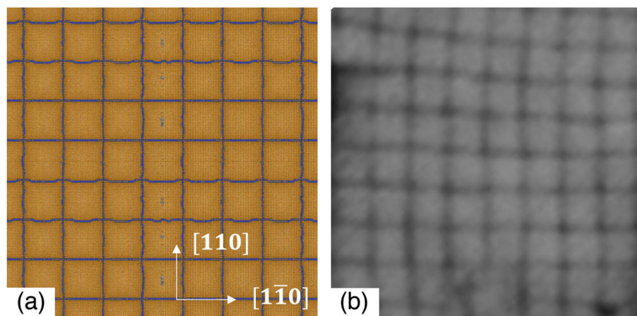

Figure 2. a) The atomic structure of a Si/Ge (001) semicoherent interface predicted in a CAC model. The orange atoms and blue lines, respectively, correspond to the pristine diamond cubic crystal structure and edge dislocations. b) A plan-view dark-field TEM image of a 20 nm thick Si/Ge (001) sample, which was annealed at 680 °C for 10 min. Reproduced with permission.[47] Copyright 2005, AIP Publishing.

result, the aforementioned reduction in the number of DOFs (96.47%) is directly related to the computational gain of the CAC simulations with respect to MD. To validate the CAC method and the interatomic potential, we build a Si/Ge (001) semicoherent interface in CAC and compare it, in **Figure 2**, against a transmission electron microscopy (TEM) image.[47] For more details of the theoretical foundation, mathematical formulation, and numerical implementation of the CAC method, the readers are referred to a recent review article.[28]

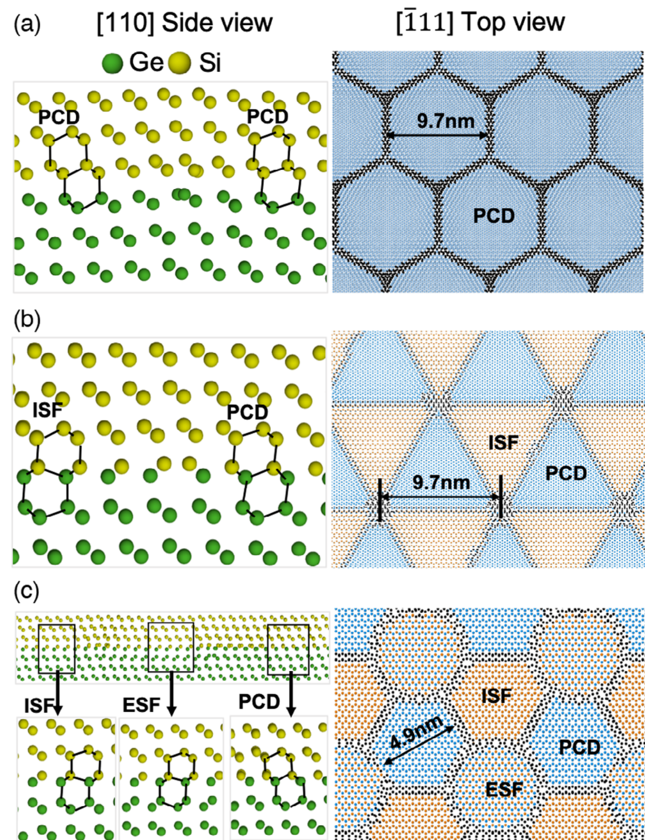

Figure 3. Atomistic configurations of three types of relaxed Si/Ge semicoherent interfaces. a), b), and c) correspond to Type I, Type II, and Type III interfaces, respectively. In the right column, local lattice structures are identified using a diamond structure identification method; atoms in black show the locations of dislocation lines identified by DXA. PCD: pristine cubic diamond; ISF: intrinsic stacking fault; ESF: extrinsic stacking fault.

3. Results and Discussion

3.1. Relaxed Structures of the Semicoherent Interfaces

Atomistic configurations of three types of Si/Ge semicoherent interfaces after dynamic relaxation of 20 ps are presented in **Figure 3**. In Type I interface, which coincides with the shuffle-set slip plane, a hexagonal network of perfect edge dislocations exists, with the Burgers vector $\mathbf{b} = (a_0/2) < 110 >$ and a periodicity of 9.7 nm. Both the Type II and Type III interfaces coincide with the glide-set slip plane, but the misfit dislocation network differs. Type II interface contains a triangular network of 90° Shockley partial dislocations, with the Burgers vector $\mathbf{b}_\mathrm{p} = (a_0/6) < 112 >$ and a periodicity of 9.7 nm. The partial dislocations are separated by intrinsic stacking faults (ISFs), which occupy 50% of the interface area. Type III interface contains a hexagonal network of 90° Shockley partial dislocations, with the same Burgers vector as Type II interface but a periodicity of only 4.9 nm, which is about half of those in Type I and Type II interfaces. The partial dislocations are separated by ISFs and extrinsic stacking faults (ESFs), each of which occupy 33.33% of the interface area. These interfacial structures are in good agreement with those found in experiments[19,21,22] and in a prior atomistic simulation.[24] The compact dislocation cores in Type I interface and the extended dislocation cores in the other two types of interface are consistent with the fact that, at low temperatures, dislocations in Si have compact and extended cores, respectively, when they are in the shuffle-set and glide-set slip planes.[48] Recent experiments and atomistic simulations found that within the Al/Si (111) interface that coincides with the glide-set slip plane in Si, there are two domains with threefold and sixfold symmetries, respectively.[49] These two domains, respectively, similar to Type II and Type III interfaces identified in our work, allow for complete relaxation of the misfit strain.

For each relaxed interfacial structure, we calculate the interface energy, which is the extra energy per area induced by the interface. We find that the interface energies are 407, 215, and 389 mJ m^{-2}, respectively, for the three types of semicoherent interfaces. These values qualitatively agree with those from a prior atomistic simulation[24] that used a different SW potential for interactions between Si and Ge:[50] 369, 272, and 349 mJ m^{-2}. Among the three types of interfaces, Type I interface has the highest energy, in line with that it is energetically favorable for an edge dislocation in a cubic diamond lattice to dissociate into two Shockley partial dislocations encompassing an ISF.[51] Type II interface attains the lowest energy, in consistent with a prior experimental observation that misfit dislocations at the Si/Ge {111} interface are primarily arranged into triangular networks.[2]

3.2. Responses of the Semicoherent Interfaces to an In-Plane Shear

With the relaxed semicoherent interfaces in hand, we first study their responses to an in-plane shear. For this purpose, the top and bottom finite elements of the bicrystal are incrementally displaced along opposite directions parallel to the $x[10\bar{1}]$ axis. Let γ be the overall strain. The strain rate $\dot{\gamma} = 3.3 \times 10^8\ s^{-1}$. We find that, when γ is small, all three misfit dislocation networks are stable. However, when γ reaches 1.32%, some misfit dislocations at Type I interface start to glide out of the traction-free boundaries. At $\gamma = 7.8\%$, the dislocation density reduces by 64.3% compared with the unsheared interface, as shown in **Figure 4**c. At the same γ, however, the misfit dislocation networks at Type II and Type III interfaces remain stable, as shown in Figure 4d,e. Evidently, when the interfaces are subject to an in-plane shear, networks of 90° partial dislocations are more stable than that of perfect edge dislocations.

3.3. Interactions between the Semicoherent Interfaces and Lattice Dislocations

Next, we investigate the interactions between lattice dislocations and different types of semicoherent interfaces. To nucleate lattice dislocations, we introduce a step of $4|\mathbf{b}|$ at the top surface of the bicrystal (Figure 1) and displace the finite elements at the step along the $-z$-direction.[52] In this way, four identical 60° lattice dislocations on $(11\bar{1})$ plane with line direction $[1\bar{1}0]$ and Burgers vector $(a_0/2)[011]$ are created. Note that the lattice dislocations are in the shuffle-set slip plane in Si and are compact. It follows that a shear strain is incrementally applied on the $[11\bar{1}]$ plane along the [011] direction to drive the dislocations to move toward the Si/Ge interface. Furthermore, let subscripts L, M, and R denote the lattice dislocation, misfit dislocation, and the dislocation formed by their reaction, respectively, and let superscripts Si and Ge denote the two materials.

At Type I interface, the first lattice dislocation reacts with the misfit edge dislocations via

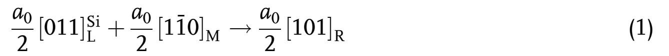

$$\frac{a_0}{2}[011]_L^{Si} + \frac{a_0}{2}[1\bar{1}0]_M \rightarrow \frac{a_0}{2}[101]_R \quad (1)$$

The resultant dislocation "R," which has a 60° character angle, is then stuck at the Si/Ge interface, as shown in **Figure 5**a. As the resolved shear strain increases, a second lattice dislocation interacts with the interface via the same reaction. Then, as a third lattice dislocation approaches the interface, the dislocation "R" is dissociated via

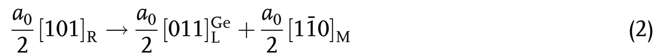

$$\frac{a_0}{2}[101]_R \rightarrow \frac{a_0}{2}[011]_L^{Ge} + \frac{a_0}{2}[1\bar{1}0]_M \quad (2)$$

The dislocation "L" then glides in Ge on the $(11\bar{1})$ plane along the $-z$-direction. We remark that, although Equation (2) seems the opposite of Equation (1), the interface is not fully recovered but distorted because of the difference in the lattice parameter a_0 between Si and Ge. It follows that the remaining three lattice dislocations react with the Si/Ge interface and glide into Ge via the same mechanism.

At Type II interface, the first lattice dislocation reacts with the misfit 90° partial dislocations via

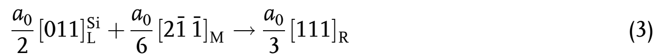

$$\frac{a_0}{2}[011]_L^{Si} + \frac{a_0}{6}[2\bar{1}\,\bar{1}]_M \rightarrow \frac{a_0}{3}[111]_R \quad (3)$$

where the resultant dislocation "R" is formed and pinned at the boundaries of the triangular ISFs, as shown in Figure 5b. As a result, the part of dislocation "L" that is aligned with the ISFs is in Si, whereas that with the pristine cubic diamond (PCD) lattices is in Ge. Similar to Type I interface, the dislocation "R" is dissociated, upon the approaching of the third lattice dislocation, via

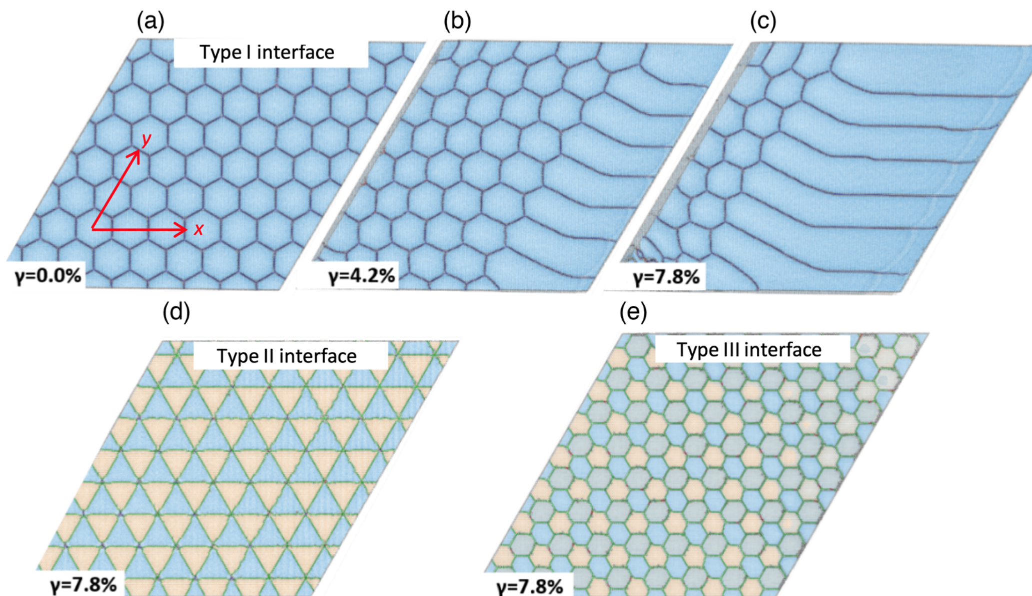

Figure 4. Atomistic configurations of three types of Si/Ge semicoherent interfaces subject to different in-plane shear strain γ. a–c), d), and e) correspond to Type I, Type II, and Type III interfaces, respectively. The in-plane shear is along the x-direction.

© 2020 Wiley-VCH GmbH

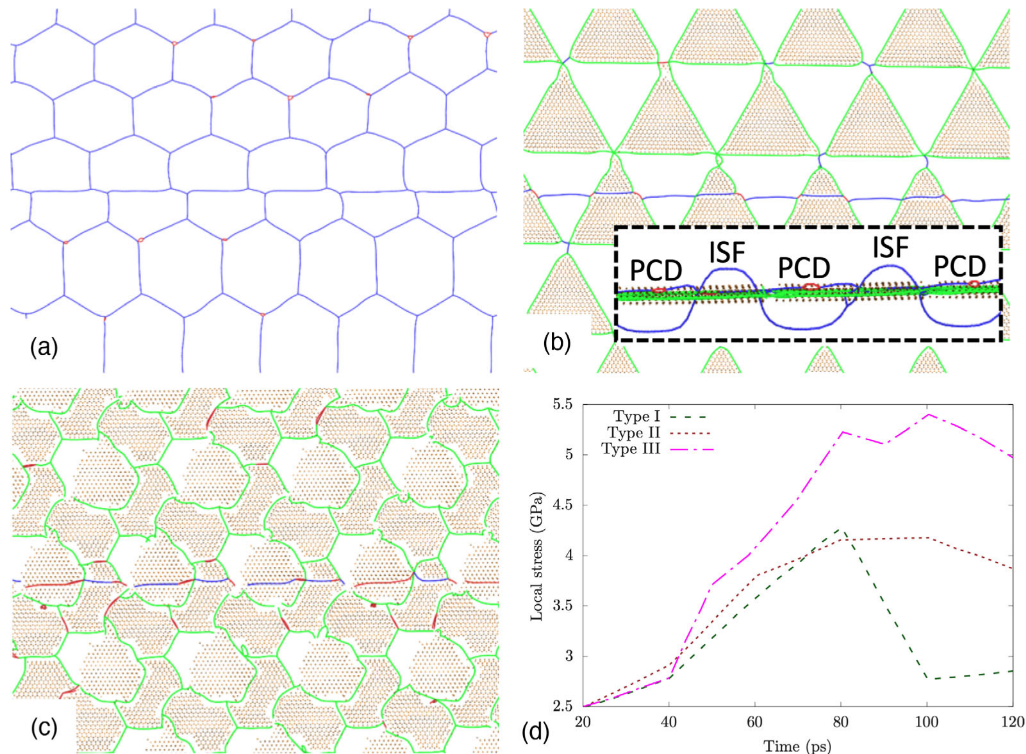

Figure 5. a–c) Atomistic configurations of a) Type I, b) Type II, and c) Type III Si/Ge semicoherent interfaces upon their interactions with the first lattice dislocation originated from Si. ISF: intrinsic stacking fault; PCD: pristine cubic diamond. d) For all three types of interfaces, the local stress component associated with the $[11\bar{1}]$ plane along the [011] direction is plotted with respect to time. The time starts at 20 ps, which is right after the dynamic relaxation and at the time the shear strain is applied to drive the dislocation motion.

$$\frac{a_0}{3}[111]_{\mathrm{R}} \rightarrow \frac{a_0}{2}[011]_{\mathrm{L}}^{\mathrm{Si}} + \frac{a_0}{6}[2\bar{1}\,\bar{1}]_{\mathrm{M}} \tag{4}$$

Then, the dislocation "L" glides in Ge on the $(11\bar{1})$ plane along the $-z$-direction. Again, similar to Type I interface, Type II interface is distorted after the transmission of each lattice dislocation owing to the difference in a_0 across the interface, with the reaction mechanism being the same for all four lattice dislocations.

At Type III interface, the reactions in Equation (3) and (4) are observed, as shown in Figure 5c. However, differing from the first two types of interfaces, the dislocation "R" here is dissociated only upon the approaching of the fourth lattice dislocation. This suggests that Type III interface impedes the gliding of lattice dislocations more significantly than the other two interfaces. Indeed, as shown in Figure 2, the PCD regions occupy only 33.33% of the interface area in Type III interface, whereas the same quantity is 99% and 50% for Type I and Type II interfaces, respectively. For a quantitative understanding, we calculate the time evolution of the Cauchy stresses on the three interfaces via a recently developed surface-based formula, using the direct physical definition of stress for force per unit area.[53–55] Figure 5d presents the component of the Cauchy stress tensor associated with the applied strain, i.e., on the $[11\bar{1}]$ plane along the [011] direction. It is found that the peak local stresses are, respectively, 4.3, 4.2, and 5.4 GPa, for the three types of interfaces. The finding that Type III interface possesses the highest peak local stress corresponds to that it is a stronger barrier to the gliding of lattice dislocations compared with the other two types of interfaces.

4. Conclusion

In this article, we analyze three types of Si/Ge (111) semicoherent interfaces in terms of their responses to an in-plane shear and interactions with lattice dislocations using CAC simulations. It is demonstrated that 1) the CAC model, with a reduction of 96.47% in the number of DOFs compared with a fully resolved atomistic model, retains the same Si/Ge interfacial structures as the latter; 2) Type I interface, which contains a hexagonal network of misfit edge dislocations, has the highest interface energy, whereas Type II interface, which contains a triangular network of misfit 90° partial dislocations, has the lowest interface energy; 3) subject to an in-plane shear, Type I interface is the least stable among the three types of interfaces; and 4) Type III interface, which contains a hexagonal network of misfit 90° partial dislocations, impedes the gliding of lattice dislocations more significantly than the other two types of interfaces, owing to its smallest percentage of the PCD region.

Acknowledgements

This material was based on research supported by the U.S. Department of Energy, Basic Energy Sciences under Award # DE-SC0006539. The work of

 © 2020 Wiley-VCH GmbH

S.X. was supported in part by the Elings Prize Fellowship in Science offered by the California NanoSystems Institute on the UC Santa Barbara campus. The works of Y.L. and Y.C. were partially supported by the National Science Foundation grant CMMI 1761512, and the computer simulations of Y.L. are funded by the Extreme Science and Engineering Discovery Environment (XSEDE) allocation TG-DMR190008. The authors thank Shengfeng Yang for implementing the SW potentials for Si and Ge in his CAC code for this project and Weixuan Li for generating some of the simulation data.

Conflict of Interest

The authors declare no conflict of interest.

Keywords

dislocation/interface interactions, germanium, in-plane shear, semicoherent interfaces, silicon

Received: May 19, 2020
Revised: August 6, 2020
Published online: August 31, 2020

[1] S. Vepřek, *J. Vac. Sci. Technol. A* **1999**, *17*, 2401.
[2] S. N. Filimonov, V. Cherepanov, N. Paul, H. Asaoka, J. Brona, B. Voigtländer, *Surf. Sci.* **2005**, *599*, 76.
[3] C. J. K. Richardson, M. L. Lee, *MRS Bull.* **2016**, *41*, 193.
[4] N. Paul, H. Asaoka, B. Voigtländer, *Surf. Sci.* **2004**, *564*, 187.
[5] J. Kim, H. Ghaffarian, S. Ryu, K. Kang, *Comput. Mater. Sci.* **2020**, *173*, 109375.
[6] T. Shimokawa, T. Niiyama, M. Okabe, J. Sawakoshi, *Acta Mater.* **2019**, *164*, 602.
[7] P. M. Anderson, S. Rao, Y. Cheng, P. M. Hazzledine, *MRS Proc.* **1999**, *586*, 267.
[8] M. A. Shehadeh, G. Lu, S. Banerjee, N. Kioussis, N. Ghoniem, *Philos. Mag.* **2007**, *87*, 1513.
[9] D. Cheng, Z. J. Yan, L. Yan, *Thin Solid Films* **2007**, *515*, 3698.
[10] Y. Zhu, Z. Li, M. Huang, *Comput. Mater. Sci.* **2013**, *70*, 178.
[11] M. Horn-von Hoegen, F. J. Meyer zu Heringdorf, M. Kammler, C. Schaeffer, D. Reinking, K. R. Hofmann, *Thin Solid Films* **1999**, *343–344*, 579.
[12] M. L. Lee, D. A. Antoniadis, E. A. Fitzgerald, *Thin Solid Films* **2006**, *508*, 136.
[13] F. C. Frank, *Acta Metall.* **1953**, *1*, 15.
[14] B. A. Bilby, R. Bullough, E. Smith, J. M. Whittaker, *Proc. R. Soc. Lond. A* **1955**, *231*, 263.
[15] S. Xu, Y. Su, *Phys. Lett. A* **2018**, *382*, 1185.
[16] J. Wang, R. Zhang, C. Zhou, I. J. Beyerlein, A. Misra, *J. Mater. Res.* **2013**, *28*, 1646.
[17] L. Zou, C. Yang, Y. Lei, D. Zakharov, J. M. K. Wiezorek, D. Su, Q. Yin, J. Li, Z. Liu, E. A. Stach, J. C. Yang, L. Qi, G. Wang, G. Zhou, *Nat. Mater.* **2018**, *17*, 56.
[18] M. Horn-von Hoegen, M. Copel, J. C. Tsang, M. C. Reuter, R. M. Tromp, *Phys. Rev. B* **1994**, *50*, 10811.
[19] H. P. Strunk, M. Albrecht, in *Defect Control in Semiconductors* (Ed.: K. Sumino), Elsevier, Oxford **1990**, pp. 1147–1151.
[20] W. Bollmann, *Crystal Defects and Crystalline Interfaces*, Springer-Verlag, Berlin, Heidelberg **1970**.
[21] P. O. Hansson, F. Ernst, E. Bauser, *J. Appl. Phys.* **1992**, *72*, 2083.
[22] F. Ernst, P. Pirouz, E. Bauser, *Phys. Status Solidi A* **1992**, *131*, 651.
[23] M. Dornheim, H. Teichler, *Phys. Status Solidi A* **1999**, *171*, 267.
[24] M. Dornheim, H. Teichler, *Phys. Status Solidi B* **2000**, *222*, 101.
[25] P. A. Pluchino, X. Chen, M. Garcia, L. Xiong, D. L. McDowell, Y. Chen, *Comput. Mater. Sci.* **2016**, *111*, 1.
[26] Y. Chen, J. Lee, *Philos. Mag.* **2005**, *85*, 4095.
[27] Y. Chen, *J. Chem. Phys.* **2009**, *130*, 134706.
[28] Y. Chen, S. Shabanov, D. L. McDowell, *J. Appl. Phys.* **2019**, *126*, 101101.
[29] S. Xu, L. Xiong, Y. Chen, D. L. McDowell, *Crystals* **2017**, *7*, 120.
[30] S. Xu, D. L. McDowell, I. J. Beyerlein, *Acta Mater.* **2019**, *174*, 160.
[31] S. Xu, M. I. Latypov, Y. Su, *Philos. Mag. Lett.* **2018**, *98*, 173.
[32] S. Xu, L. Xiong, Y. Chen, D. L. McDowell, *J. Mech. Phys. Solids* **2016**, *96*, 460.
[33] S. Xu, L. Xiong, Y. Chen, D. L. McDowell, *Acta Mater.* **2017**, *122*, 412.
[34] S. Xu, *Int. J. Multiscale Comput. Eng.* **2018**, *16*, 367.
[35] S. Yang, N. Zhang, Y. Chen, *Philos. Mag.* **2015**, *95*, 2697.
[36] L. Xiong, D. L. McDowell, Y. Chen, *Scr. Mater.* **2012**, *67*, 633.
[37] Y. Li, Z. Fan, W. Li, D. L. McDowell, Y. Chen, *J. Mater. Res.* **2019**, *34*, 2306.
[38] S. Xu, L. Xiong, Y. Chen, D. L. McDowell, *npj Comput. Mater.* **2016**, *2*, 15016.
[39] S. Xu, L. Xiong, Y. Chen, D. L. McDowell, *JOM* **2017**, *69*, 814.
[40] F. H. Stillinger, T. A. Weber, *Phys. Rev. B* **1985**, *31*, 5262.
[41] K. Ding, H. C. Andersen, *Phys. Rev. B* **1986**, *34*, 6987.
[42] M. Laradji, D. P. Landau, B. Dünweg, *Phys. Rev. B* **1995**, *51*, 4894.
[43] A. Stukowski, V. V. Bulatov, A. Arsenlis, *Modell. Simul. Mater. Sci. Eng.* **2012**, *20*, 085007.
[44] A. Stukowski, *Modell. Simul. Mater. Sci. Eng.* **2010**, *18*, 015012.
[45] S. Xu, L. Xiong, Q. Deng, D. L. McDowell, *Int. J. Solids Struct.* **2016**, *90*, 144.
[46] S. Xu, T. G. Payne, H. Chen, Y. Liu, L. Xiong, Y. Chen, D. L. McDowell, *J. Mater. Res.* **2018**, *33*, 857.
[47] A. Sakai, N. Taoka, O. Nakatsuka, S. Zaima, Y. Yasuda, *Appl. Phys. Lett.* **2005**, *86*, 221916.
[48] Z. Li, R. C. Picu, *J. Appl. Phys.* **2013**, *113*, 083519.
[49] X.-Y. Liu, I. Arslan, B. W. Arey, J. Hackley, V. Lordi, C. J. K. Richardson, *ACS Nano* **2018**, *12*, 6843.
[50] M. Ichimuraa, J. Narayan, *Philos. Mag. A* **1995**, *72*, 281.
[51] S. Z. Chavoshi, S. Xu, X. Luo, *Mater. Sci. Semicond. Process.* **2016**, *51*, 60.
[52] X. Chen, L. Xiong, A. Chernatynskiy, Y. Chen, *J. Appl. Phys.* **2014**, *116*, 244309.
[53] Y. Chen, *Europhys. Lett.* **2016**, *116*, 34003.
[54] Y. Chen, A. Diaz, *Phys. Rev. E* **2016**, *94*, 053309.
[55] Y. Chen, A. Diaz, *Phys. Rev. E* **2018**, *98*, 052113.

© 2020 Wiley-VCH GmbH